nature communications

Article

https://doi.org/10.1038/s41467-025-57618-8

Orbital angular momentum control of strong-field ionization in atoms and molecules

Received: 30 July 2024

Accepted: 21 February 2025

Published online: 12 March 2025

Check for updates

Jean-Luc Bégin, Ebrahim Karimi, Paul Corkum, Thomas Brabec & Ravi Bhardwaj

Tunnel ionization, the fundamental process in strong field physics and attosecond science, along with the subsequent electron dynamics are typically governed by the polarization and carrier envelope phase of the incident laser pulse. Moreover, most light-matter interactions involve Gaussian beams and rely primarily on dipole-active transitions. In this article, we reveal that Orbital Angular Momentum (OAM) carrying beams enable to control tunnel ionization in atoms and molecules. The ionization process is manipulated by the sign and value of the OAM and by displacing the phase singularity. We show that the helical phase and field gradients inherent in the higher-order multipole expansion of the tunneling process cause ionization to depend on OAM. Simulations indicate that, in contrast to Gaussian beams, the ponderomotive effects can also be controlled with OAM and the asymmetry in the optical vortex. Our findings have an impact on attosecond science, spectroscopy, and super-resolution microscopy.

Our current understanding of light-matter interactions stems from photo-excitation using Gaussian beams, which closely approximate plane waves and rely primarily on dipole-active transitions. The spatial disparity between atom size and light wavelength typically renders higher multi-polar effects insignificant, thereby justifying the widespread use of the dipole approximation. However, light beams can be structured to introduce spatial inhomogeneities in the field parameters such as frequency, amplitude, polarization, and phase[1,2]. These structured light beams possess additional degrees of freedom that profoundly influence their interaction with matter, driving advancements in both fundamental studies and practical applications. Among a plethora of optical fields that can be generated, optical vortex beams that carry OAM, $l\hbar$ per photon, with respect to the vortex axis, have garnered widespread use across diverse research areas ranging from particle trapping and manipulation[3,4] to quantum entanglement[5,6], quantum information processing[7,8], super-resolution imaging[9], and laser material processing[10–13]. Here, l is an integer number and $\hbar$ is the reduced Planck constant. In such beams, the phase changes across the beam profile, resulting in a phase singularity and a null intensity at the center. The resultant wavefront undergoes l-intertwined rotations in a wavelength describing a corkscrew pattern with defined handedness; these beams are also known as helical or twisted light beams.

With structured light, the validity of the dipole approximation becomes uncertain due to the presence of OAM and field gradients. Typically, the first-order dipole approximation fails when the wavelength is comparable to the spatial extent of bound states, or when the electron velocity becomes a fraction of the speed of light, making it susceptible to the Lorentz force from the magnetic field component. The former limit is reached for X-rays, while the latter occurs at high laser intensities and long wavelengths[14,15]. In the next order, magnetic dipole and electric quadrupole terms become relevant in the light-matter interactions. The magnetic dipole term opens new pathways for atomic and molecular transitions[16] (including ionization), while the electric quadrupole term, which depends on the field gradient, contributes to effects such as the ponderomotive force. Electric quadru-

Nexus for Quantum Technologies, Department of Physics, University of Ottawa, Ottawa, ON, Canada. e-mail: jbegin2@uottawa.ca; thomas.brabec@uottawa.ca; ravi.bhardwaj@uottawa.ca

https://doi.org/10.1038/s41467-025-57618-8

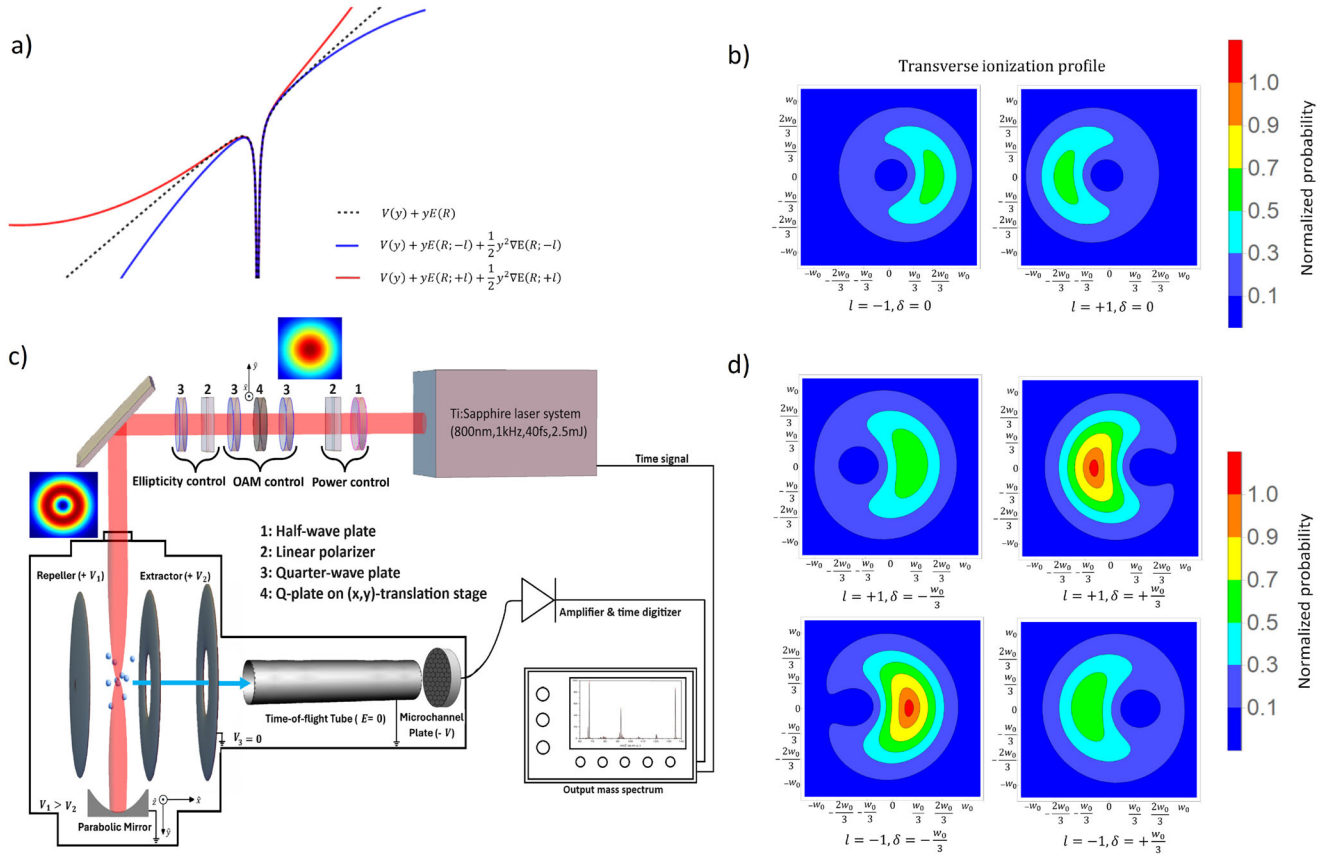

Fig. 1 | OAM-dependent ionization in atoms. a Distortion of atomic potential at peak intensity for a vertically polarized Gaussian beam (black dashed line) and, for $l = -1$ (blue) and $l = +1$ (red) LG beams. The potentials were evaluated with the beam coordinates at $(\frac{w_0}{3}, 0)$ μm for $\delta = -w_0/3$. **b** Normalized transverse profiles of ionization probability for symmetric ($\delta = 0 \mu m$) LG beam with $l = -1$ (left panel) and $l = +1$ (right panel). **c** Schematic of the experimental layout showing the optics used in the generation of OAM beams and the measurement of ion yields using time-of-flight mass spectrometer. **d** Normalized transverse profiles of ionization probability for asymmetric LG beam when the singularity is displaced to either side of the center by $\delta = \pm \frac{w_0}{3}$ for $l = +1$ (top panels) and $l = -1$ (bottom panels). Ionization probabilities were evaluated at an intensity of 10^{14} W/cm^2, and the x and y-axis are given in terms of the beam waist, $w_0 = 3$ μm.

pole transitions, which are rarely observed in plane wave illumination, have been shown recently to play a prominent role in photoabsorption[17,18]. Additionally, the transfer of OAM to the bound electron has been found to modify the selection rules for atomic transitions in trapped ions[19–21].

In the realm of extreme nonlinear optics, intense near-infrared light pulses have been used to generate (i) extreme ultraviolet photons with spatio-temporal control of OAM[22–24] and (ii) spatiotemporally tailored terahertz pulses called "flying donuts" using bichromatic light fields and metasurfaces[25,26]. Despite these advancements, the precise influence of OAM and field gradients on photoionization, the primary step in such a nonlinear process, remains elusive. Furthermore, the ability to manipulate light-matter interactions holds significant potential. Conventional methods have achieved limited control over strong field ionization employing techniques such as varying the carrier envelope phase of a few-cycle pulse[27], pulse shaping[28], coherent control[29,30], and using bichromatic light fields[31].

In this article, we demonstrate enhanced control and tunability of strong-field ionization by altering the phase and field gradient of structured light. We show that the strong-field ionization of atoms and molecules (a) is influenced by the value and sign of OAM and (b) can be substantially manipulated by displacing the phase singularity in the vortex beam. Ion yields increase significantly for a specific handedness of helical light, exhibiting the opposite behavior for the other handedness. This selective ionization leads to helical dichroism in both atoms and molecules and can be precisely controlled. We simulate the ionization behavior of argon atoms by extending the Strong-Field Approximation (SFA) beyond the dipole approximation, incorporating the contribution of multipole moments during tunnel ionization for an asymmetric Laguerre-Gaussian (LG) beam. We show that the OAM dependence of tunnel ionization is induced by the phase singularity of the LG beam, which causes variations in the distortion of the atomic potential depending on the handedness of helical light. This effect is further amplified by the field gradient in asymmetric LG beams, enabling control and enhancement of both the peak ponderomotive energy and the average ponderomotive force. Finally, we demonstrate localization of light intensity to subwavelength dimensions. This level of control and tunability over ionization and electron energy opens up new opportunities in spectroscopy, attosecond science, plasma physics and imaging, some of which are explored in detail later in this article.

Results

The basic concept of OAM-dependent ionization is illustrated in Fig. 1a by considering the distortion of the atomic potential

caused by the incident light field. For a Gaussian beam, the atomic potential is tipped by the applied electric field (black dotted curve in Fig. 1a), allowing the electrons to tunnel through the barrier. This non-resonant strong-field ionization is significantly influenced by the peak of the laser field. This conventional picture does not include higher-order multipole effects. Beyond the dipole approximation, the electric quadrupole term depends on the field gradient (∇E). For LG beam, the transverse profile in Cartesian coordinates is given by

$$\mathbf{E}^{\pm}_{0,l}(x,y,z) = E_0 \frac{w_0}{w(z)} \left(\frac{\sqrt{2}}{w(z)}\right)^{|l|} [(x \pm iy)]^{|l|} \exp\left[-\frac{r^2}{w^2(z)}\right] \exp\left[ikz - ik\left(\frac{r^2}{2R(z)}\right) + i(|l|+1)\psi(z)\right] \quad (1)$$

where the handedness of the helical phase is represented by the $\pm$, $|l|$ is the azimuthal index, the radial index is set to zero $p = 0$, E_0 is the field amplitude, $w(z)$ is the beam waist, $r = \sqrt{x^2+y^2}$, k is the wave number, $R(z)$ is the radius of curvature, and $\psi(z)$ is the Gouy phase. Taking a gradient of this field leads to a factor of $\pm|l|$ that either enhances or reduces the potential distortion (blue and red curves in Fig. 1a). Helicity-dependent distortion of atomic potential is purely a phase effect and does not exist in non-OAM beams.

To understand the origin of OAM-dependent ionization, we considered the SFA of tunnel ionization and extended it to include contributions from multipole moments for an asymmetrical LG beam. In the standard SFA model, the transition amplitude from the ground to the final state, in atomic units, is given by refs. 32,33

$$M_{fg} = -i\int_{-\infty}^{t} \langle \psi_V(t')|V(t')|\psi_g(t')\rangle dt', \quad (2)$$

where $V(t')$ is the interaction Hamiltonian within dipole approximation, $|\psi_g(t')\rangle$ is the ground state wavefunction, and $\langle\psi_V(t')|$ is the Gordon-Volkov continuum wavefunction, which is a plane wave modulated by the laser field.

To introduce higher-order multipoles in the interaction Hamiltonian, we Taylor expanded the vector potential to the second order about a point R in the velocity gauge and transformed it to the length gauge to obtain $\hat{V}(t') = r_i E_i(R,t') + \frac{1}{2} r_i r_j \widehat{\partial_j E_i}(R,t') + \frac{1}{2} L_i B_i(R,t')$, where $E_i(R,t)$ and $B_i(R,t)$ are the incident electric and magnetic fields of the asymmetrical LG laser beam (see Supplementary section 6), $r_{i,j}$ is the coordinates of the quadrupole moment i.e. the distance between positive and negative charge in the atom frame, and R represent the coordinates of the laser beam profile. $\widehat{\partial_j E_i}$ represents the field gradient tensor and L_i is the orbital angular momentum of the magnetic dipole transition moment.

The expanded Gordon-Volkov wavefunction that includes the higher order multipoles is therefore given by

$$\Psi_V(r,t) = \frac{1}{(2\pi)^{3/2}} e^{i\left(p + A(R,t') - \int_{t'}^{t} \widehat{\partial_R A}(R,\tau)(p+A(R,\tau))d\tau\right)\cdot r} \times e^{-\frac{i}{2}\int_{t'}^{t}\left(p + A(R,t'') - \int_{t''}^{t} \widehat{\partial_R A}(R,\tau)(p+A(R,\tau))d\tau\right)^2 dt''}, \quad (3)$$

where $A(R,t)$ is the vector potential of the laser field, p is the electron momentum and $\widehat{\partial_R A}(R,t)$ is the vector potential gradient tensor (see Supplementary section 5). Within the dipole approximation, the field gradient tensor term does not exist in the Gordon-Volkov wave function.

The full transition amplitude used to describe the tunnel ionization probability is given by

$$M_{fg} = -i\int_{-\infty}^{t} \left[\underbrace{\langle \pi(p,t,t')|r_i|\psi_g\rangle E_i(R,t')}_{\mathrm{E1}} + \underbrace{\frac{1}{2}\langle \pi(p,t,t')|r_i r_j|\psi_g\rangle \widehat{\partial_j E_i}(R,t')}_{\mathrm{E2}} + \underbrace{\frac{1}{2}\langle \pi(p,t,t')|L_i|\psi_g\rangle B_i(R,t')}_{\mathrm{M1}} \right] \times \exp\left(\frac{i}{2}\int_{t'}^{t}\left(\pi^2(p,t,t'') + 2I_p\right)dt''\right)dt', \quad (4)$$

where

$$\pi(p,t,t'') = p + A(R,t'') - \int_{t''}^{t} \widehat{\partial_R A}(R,\tau)(p+A(R,\tau))d\tau. \quad (5)$$

Equation (4) consists of three terms: M_{fg}^{E1}, M_{fg}^{E2}, and M_{fg}^{M1} which are the electric dipole, electric quadrupole, and magnetic dipole transitions, respectively. The probability of transition is given by

$$P_{fg} = \left| M_{fg}^{\mathrm{E1}} + cM_{fg}^{\mathrm{E2}} + M_{fg}^{\mathrm{M1}} \right|^2. \quad (6)$$

The probability contains a weighting factor c to adjust the relative strength of the electric quadrupole transitions. Both magnetic dipole and electric quadrupole transitions are typically ~ 10^{-5} - 10^{-6} times weaker compared to dipole transitions[34], with their strength scaling inversely with the square of the fine structure constant. However, the electric quadrupole moments of atoms are known to be greatly enhanced by a few orders due to the hyperfine interaction of atomic electrons with the nucleus[35–37]. The weighting factor c was obtained by taking the ratio, $c = Q/Q_N$, where $Q = Q_N + Q_\mu + Q_Q$ is the total quadrupole moment of the atom, Q_N is the nuclear quadrupole moment and Q_μ (Q_Q) is the induced quadrupole moment due to the hyperfine interaction between the electron and magnetic dipole (electric quadrupole) of the nucleus. Our model, based on SFA, does not take into account the influence of nucleus on the energy levels, thereby, ignoring the hyperfine interactions. As a result, higher c − values are required for quantitative analysis.

To simulate the transverse ionization probability profile, we used the ground state 3p-orbital of argon and the electric field represented by the LG beam (Eq. (1), also see Supplementary Section 6), and solved the electric dipole, magnetic dipole, and electric quadrupole transition matrix elements in momentum space represented by canonical momentum $\pi(p,t,t')$ with c = 200. For argon 3p state, the c-value varies within the order of 10^2-10^3 for a total atomic angular momentum of $F = I \pm 1/2$ and $F = I \pm 3/2$. The resulting time component of the transition from ground to the continuum was evaluated using saddle point integration (see Eqs. (28)–(33) in Methods for theory).

Figure 1 b shows the transverse ionization probability profile for $l = \pm 1$ at $\delta = 0$. The average ionization probability is identical for left- and right-helical light. However, a horizontal cut across the beam cross-section reveals an asymmetry in the distribution, with a greater presence on the left (right) for $l = +1$ ($l = -1$). Figure 1b suggests that probing the ionization locally would display an asymmetry in angular distribution of electrons akin to that observed in photoelectron circular dichroism experiments[38,39], albeit with linearly polarized helical light beams. However, spatial averaging over the beam cross-section causes the field gradient term to vanish. So, for symmetric LG beams, the total ion yields are expected to be independent of helicity of light and comparable to a Gaussian beam.

The effect of spatial averaging can be negated by displacing the singularity from the center of the beam to generate asymmetric LG

beams. Experimentally, such beams can be produced by translating a phase plate used to generate OAM beams perpendicular to the incident Gaussian beam (Fig. 1c and Methods section 1.3) or by the coherent superposition of Gaussian and LG beams[12]. Theoretically, an asymmetrical LG beam is given by

$$\mathbf{E}^{\pm}_{0,l}(x,y,z) = E_0 \frac{w_0}{w(z)} \left(\frac{\sqrt{2}}{w(z)}\right)^{|l|} [(x \pm i\eta\delta) \pm i(y \mp i\zeta\delta)]^{|l|} \exp\left[-\frac{r^2}{w^2(z)}\right] \times \exp\left[ikz - ik\left(\frac{r^2}{2R(z)}\right) + i(|l|+1)\psi(z)\right] \quad (7)$$

where δ is the displacement of the singularity that can take both negative and positive values and η, ζ are used to displace the singularity anywhere in the x-y plane with values between 0 and 1 (See Supplementary Section 6). In asymmetric LG beams, the field gradient for both handedness at a specific position of the singularity (δ-position) are different ($\widehat{\nabla_j E_i}(+l, \pm\delta) \neq \widehat{\nabla_j E_i}(-l, \pm\delta)$) and survive spatial averaging. The field gradients amplify the l-dependent distortion of the atomic potential (Fig. 1a), enabling to manipulate the rate of ionization by displacing the phase singularity.

Figure 1 d shows transverse profiles of ionization probabilities for asymmetric LG beams when the singularity is displaced to either side of the center. Compared to symmetric LG beams (Fig. 1b), the asymmetry in the angular distribution of ionization disappears for asymmetric LG beams. However, the average ionization probability is modulated by changing the handedness of the helicity of light and scales with higher l-values. At $\delta = -w_0/3$, the average ionization probability is greater for $l = -1$ relative to $l = +1$. The trend reverses for $\delta = +w_0/3$, with $l = +1$ producing higher ionization compared to $l = -1$. In the absence of the helical phase, synthesized light fields with strong field gradients would not induce strong modulation of ionization. The key advantage of OAM beams is the handedness of the helical phase that enables to suppress/enhance ionization. While phase singularity remains crucial even in asymmetric LG beams, the field gradients enable to overcome the effect of spatial averaging, leading to the observation of OAM-dependent ionization yields.

To probe OAM-dependent strong-field ionization of atoms and molecules, we measured the ion yields using time-of-flight mass spectrometer (TOFMS). Figure 1c shows the schematic of the experimental setup. Near-infrared femtosecond laser pulses are focused by a parabolic mirror inside a differentially pumped vacuum chamber. The ions produced in the interaction region were accelerated towards a field-free drift region and are subsequently detected by microchannel plates in chevron geometry. The ion signal was then amplified, discriminated, and recorded by a time digitizer to generate a TOF mass spectrum (see Supplementary Fig. S4). A q-plate was used to convert the incident Gaussian beam to an OAM beam via spin-orbit coupling. Optical components such as waveplates and polarizers were used to control the incident power and laser polarization. Translating the q-plate with respect to the incident beam generated asymmetric OAM beams in which the phase singularity (and hence the null intensity region) is displaced within the focal spot (See Methods for experimental details).

Figure 2 shows the experimental results of the ionization of argon atom for $l = \pm 1$ (a, b) and $l = \pm 3$ (c, d) as a function of the position of the singularity, δ. For a symmetric OAM beam ($\delta = 0$), the singly charged ion yields are identical for left- and right-handed helical light (Fig. 2a, c). When the singularity is displaced to $+\delta$, the ion yields for $+l$ (black curve) increase and reach a maximum. When the handedness is changed to $-l$ (red curve), the ion yields are maximum at $-\delta$. Therefore, the δ-dependence of the ion yields for $-l$ mirrors that of $+l$ about $\delta = 0$. At higher l-values, the ratio of the maximum ion yields at $\delta \neq 0$ to the ion yields at $\delta = 0$ increase for a specific handedness of the helical light (Fig. 2a, c). The increase in the ion yields for an asymmetric OAM beam arises from the growing peak field strength and the difference in the field gradient as the singularity is displaced (refer to Fig. 1). However, at large δ positions, the ion yields decrease because of the diminishing peak field strength as the beam profile starts resembling a Gaussian-like beam (see Supplementary Fig. S12). At a specific δ-position, the difference in ionization between the left- and right-helical light persists up to saturation intensity (see Supplementary Fig. S6). The degree of control achieved using asymmetric OAM beams is significantly higher, by two orders of magnitude, when compared to conventional pulse shaping techniques[27–29] that typically operate mostly within dipole approximation.

Selective ionization with linearly polarized asymmetric helical light of opposite handedness leads to dichroism - a property typically observed in chiral molecules with broken symmetry. In our case, the interplay between the helicity of light and the broken symmetry, introduced by the δ-parameter, results in a differential response of argon. Figure 2b, d illustrate differential ionization in argon, for $l = 1, 3$, respectively, when subjected to linearly polarized helical light of opposite handedness. This difference, denoted as $\Delta Y(l) = Y(+l, s = 0) - Y(-l, s = 0)$, is known as Helical Dichroism (HD) and exhibits a characteristic sinusoidal shape. This phenomenon is akin to the recently observed nonlinear absorption of helical light in chiral and achiral liquids and solids[17,18]. As δ increases, ΔY will rise to a maximum around $\delta = \pm w_0/3$ for $l = 1$ and decrease at the large δ-position. This is because as the position of the singularity approaches the periphery of the beam's cross-section it starts to resemble a symmetric Gaussian beam profile. Notably, in Fig. 2d the difference in the yields $\Delta Y(l = 3)$ is maximum at a larger δ-position and exhibits an intriguing feature around $\delta = 0$, resembling an inflection point. This behavior is affected by the incident intensity and arises because the size of the singularity is greater for $l = 3$ relative to $l = 1$, necessitating a larger displacement to observe an appreciable increase in the ion yield.

The phenomenon of OAM-dependent ionization is not confined to atoms but also extends to molecules. Figure 3a, c show how the singly charged ion yields vary with the singularity position (δ) for $l = \pm 1$ in two molecules: R(+)-limonene (chiral molecule) and acetone (achiral molecule). In chiral systems, the two enantiomers that are non-superimposable mirror images, are discernible only when they interact with another chiral system. A typical optical probe exploits the broken symmetry of the handedness of circularly polarized light resulting in differential absorption of left- and right-handed polarizations, leading to circular dichroism. However, enhanced chiral sensitivity was achieved recently in chiral liquids and solids[17,18] by transferring this broken symmetry to the helical phase of the light rather than its polarization. In achiral systems, the conventional understanding is that dichroism does not occur due to the presence of S_n symmetry. However, achiral liquids and solids exhibited dichroism when irradiated with asymmetric OAM beams, where the symmetry is broken spatially in the beam profile and the phase of light. This raises the question of whether helical dichroism can also be observed in the gas phase.

For both molecules, the δ-dependence of ion yields for $-l$ mirrors that of the $+l$ about $\delta = 0$, similar to argon. The ion yields are identical at $\delta = 0$, and this mirroring behavior was also present for the ionization of limonene with higher-order l-values (See Supplementary Fig. S7a). Unlike argon, both molecules display an asymmetric double bump structure for a specific handedness of helical light. This is likely due to differences in their ionization potentials (8.5 eV for limonene, 9.7 eV for acetone, and 15.6 eV for argon). The double bump feature is influenced by the laser intensity and the strength of the E1E2 coupling term (see Supplementary Fig. S1a, b) and becomes more pronounced with increasing intensity approaching saturation. Strong field ionization with OAM beams is a consequence of the interplay between peak field strength and field gradients. The latter gives rise to helicity-

https://doi.org/10.1038/s41467-025-57618-8

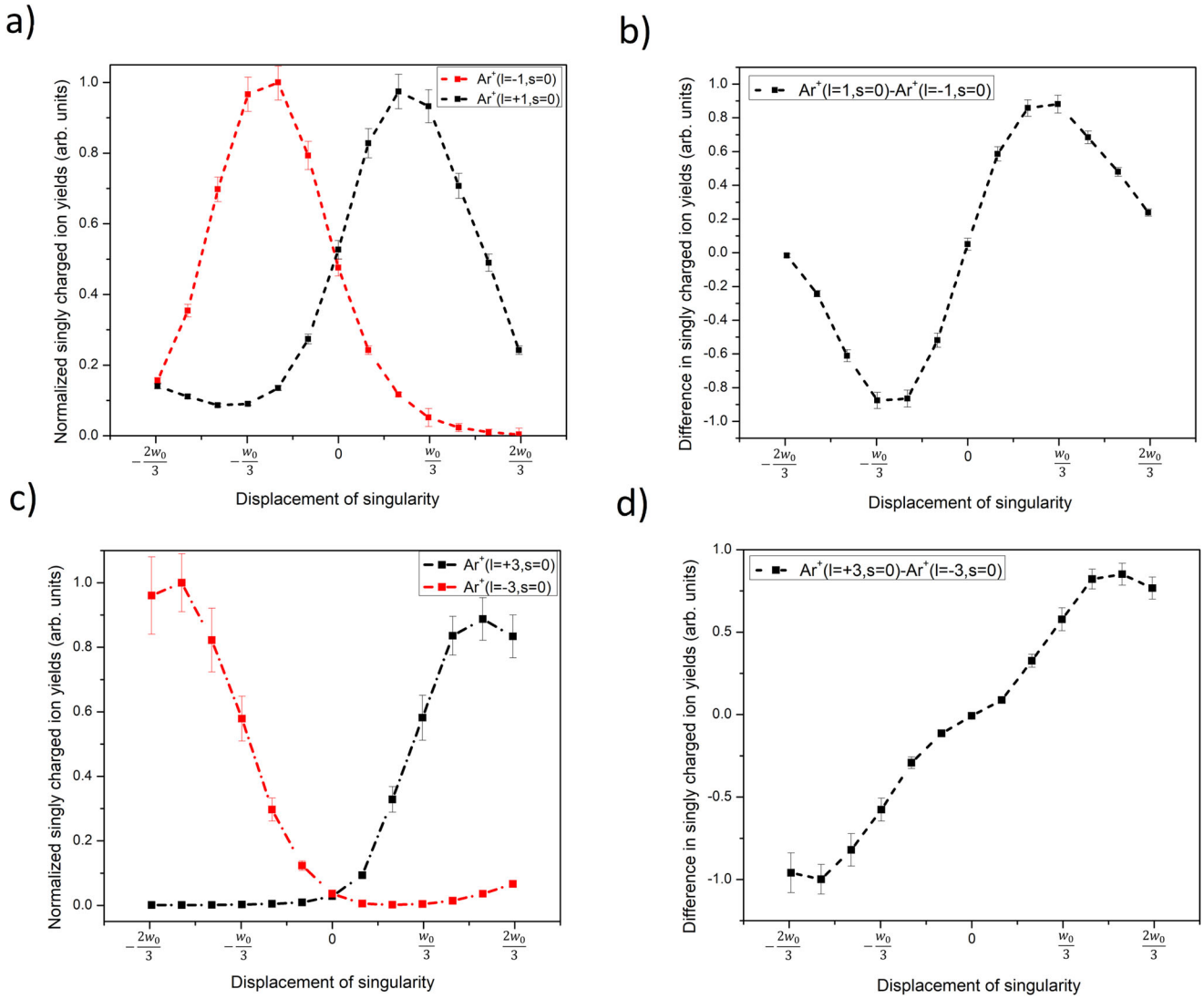

Fig. 2 | OAM control of ionization of argon atom. a Single ionization yields of argon for $l = +1$ (black) and $l = -1$ (red). **b** Difference in ionization between left- and right-handed helical light ($l = 1$). **c** Single ionization yields of argon for $l = +3$ (black) and $l = -3$ (red). **d** Difference in ionization between left- and right-handed helical light ($l = 3$). The laser polarization was linear ($s = 0$) and the intensity for $l = 1$ was 10^{14} W/cm^2 and $l = 3$ was 1.5×10^{14} W/cm^2. The x and y-axis are given in terms of the beam waist, $w_0 = 3$ μm. The error bars represent the standard error of multiple measurements ($n = 3$).

dependent ionization, while the former determines the overall ionization rate. At laser intensities approaching saturation, the peak field strength dominates the gradient contribution, leading to higher ionization rates but reduced differences in ionization between the left- and right-handed helical light (see Supplementary Fig. S6 insets) due to ground state depletion. At intensities well below saturation, the field gradient contribution dominates and has a greater impact on the helicity-dependent ionization rate. As a result, one handedness of helical light can completely suppress ionization, eliminating the asymmetrical double bump feature. In molecules, the experimental intensities used (8–9 $\times 10^{13}$ W/cm^2) were closer to their saturation intensities compared to argon.

Figure 3 b, d show HD in R(+)-limonene (see Supplementary Fig. S5 for S(−)-limonene) and in acetone, respectively, when subjected to linearly polarized helical light of opposite handedness, exhibiting the same sinusoidal shape as shown in Fig. 2b. Similar results were obtained when the laser polarization was changed from linear to circular (see Supplementary Fig. S8). For a specific δ position, the ion yields are predominant for one handedness irrespective of the ellipticity, ε, of light (see Supplementary Figs. S9, S10). For higher order l-value, limonene exhibits a similar inflection point as argon (Fig. 2d), as shown in Fig. S7b in the Supplementary. For a specific enantiomer, left- and right-handed helical light produced different ion yields. However, for a specific helicity of light, the ion yields remained similar for the two enantiomers (see Supplementary Fig. S5) within the experimental errors, in contrast to the enhanced chiral sensitivity observed in liquids and solids[17,18]. For the intensities used in the experiments, tunnel ionization is predominant where the electron transitions mostly from the ground state to continuum and does not involve the chiral-sensitive excited states. Therefore, the ionization rates are expected to be similar for both enantiomers, albeit in different directions. So, probing the electron angular distributions would provide more chiral sensitivity than the total ion yields.

To simulate the experimental results (Figs. 2, 3), we plotted the electric transition probability (Eq. (6)) integrated over the beam cross-section, given by $\overline{P}_{fg} = \int_{-w_0}^{w_0} |M_{fg}^{E1} + cM_{fg}^{E2} + M_{fg}^{M1}|^2 dR$. The only coupling term that contains $l-$ dependence is the E1E2 term due to the presence of the field gradient. The mixed coupling term E1M1 is responsible for

https://doi.org/10.1038/s41467-025-57618-8

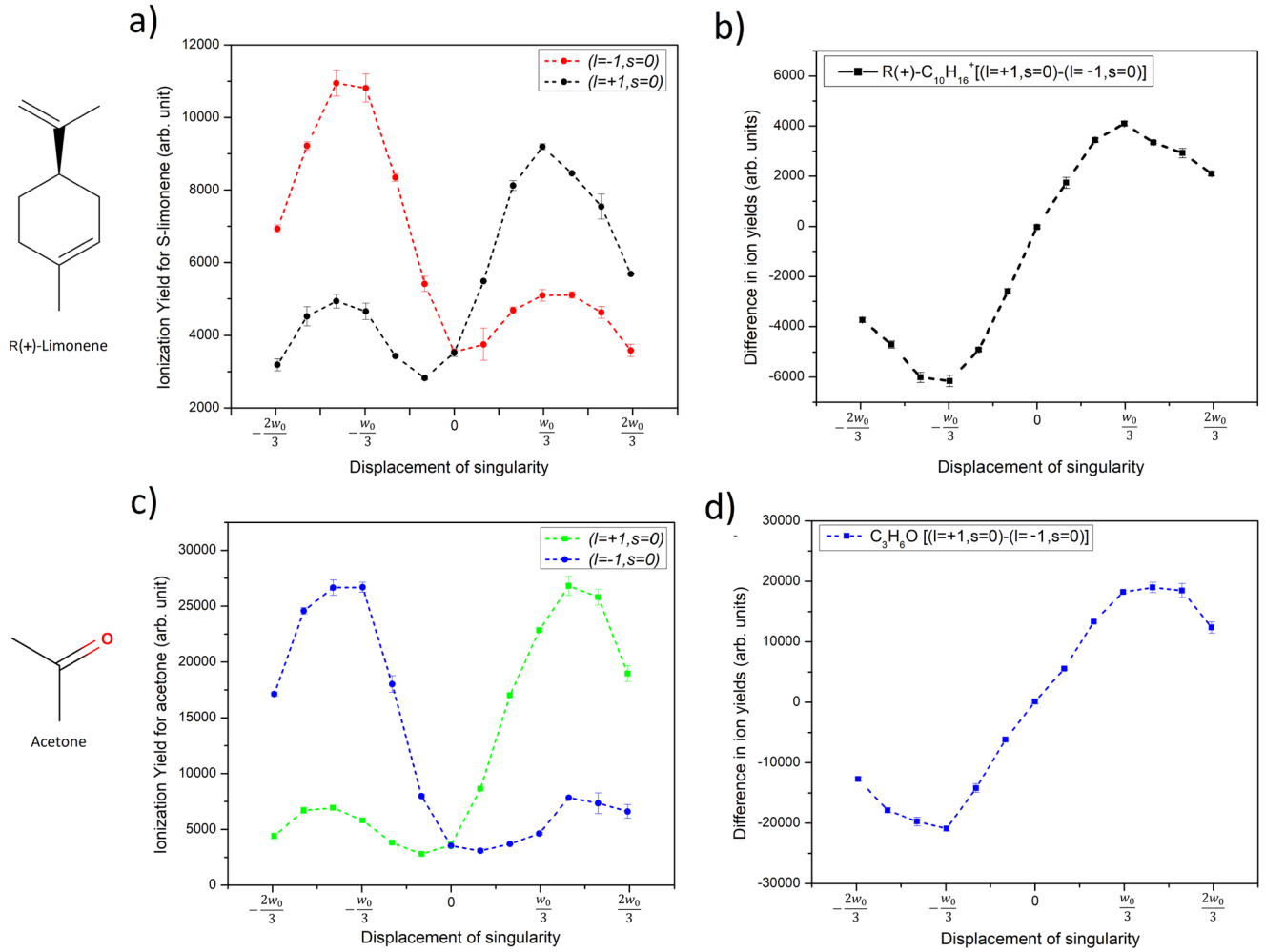

Fig. 3 | OAM-dependent ionization in molecules. Single ionization yields for $l = +1$ and $l = -1$ as a function of displacement of the singularity in (**a**) R(+)-limonene, (**c**) acetone. (**b**), (**d**) shows the difference in the ionization yields between the left- and right-helical light for the respective molecules. The laser polarization was linear ($s = 0$), and the intensity was 8×10^{13} W/cm^2 and 9×10^{13} W/cm^2 for limonene and acetone, respectively. The x and y-axis are given in terms of the beam waist, $w_0 = 3$ μm. The error bars represent the standard error of multiple measurements ($n = 3$).

circular dichroism and does not contribute to the differential signal for linearly polarized light.

Figure 4 a depicts the differential ionization probability between left- and right-helical light as a function of displacement of the singularity for $l = \pm 1$ and ± 3. These probabilities, obtained at $c = 1$, mirror the experimental results shown in Figs. 2b, d and 3b, d. For higher l − values, the null intensity region is larger, leading to stronger field gradients and higher peak field strengths. Consequently, differential ionization is enhanced but exhibits an inflection point around $\delta = 0$, accompanied by a change in the slope, as larger displacements of the singularity are required to significantly alter the ion yield. This inflection point becomes more pronounced at higher laser intensities.

While the behavior of differential ionization with the asymmetry parameter δ is independent of the c − value, visualization and comparison of ionization probabilities with experimental ion yields from Fig. 2a, c necessitate amplifying quadrupole transitions. Figure 4b illustrates the dependence of ionization probability on the displacement of the singularity for different l − values using $c = 200$, chosen to show the double bump feature that also depends on the laser intensity (Supplementary Fig. S1a). The ionization as a function of δ − position exhibits an asymmetric double bump structure. This asymmetry increases with l − value, laser intensity and c − value (see Supplementary Fig. S1a, b). It vanishes at low intensities and becomes prominent at higher intensities until the ground state is depleted. Moreover, the symmetry of the double bump structure is affected by the angle through which the singularity is displaced across the center (see Supplementary Fig. S2). A quantitative comparison of the ionization probability with the experimental results of Fig. 2a, c could be obtained for $c = 400$ or higher (see Supplementary Fig. S1b). This c-value is within the range of two to three orders of magnitude of the quadrupole moment enhancement due to the hyperfine interactions.

Discussion

The subtle differences in the distortion of the atomic potential shown in Fig. 1, induced by left- and right-handed OAM beams, give rise to intriguing phenomena in strong-field physics. They have the potential to imprint characteristic features on the angular distribution of the ionized electron with a preferred directionality by changing either the handedness of helical light or the sign of δ-position. When extended to chiral molecules, the asymmetry in the molecular potential could increase/decrease the photoelectron emission along a particular direction. This can lead to efficient chiral discrimination, analogous to photoelectron circular dichroism, and be further enhanced through the utilization of higher l-values. Moreover, the directionality of the ejected electron can be controlled by angular rotation of the singularity in the transverse plane of the laser focus. This capability provides

https://doi.org/10.1038/s41467-025-57618-8

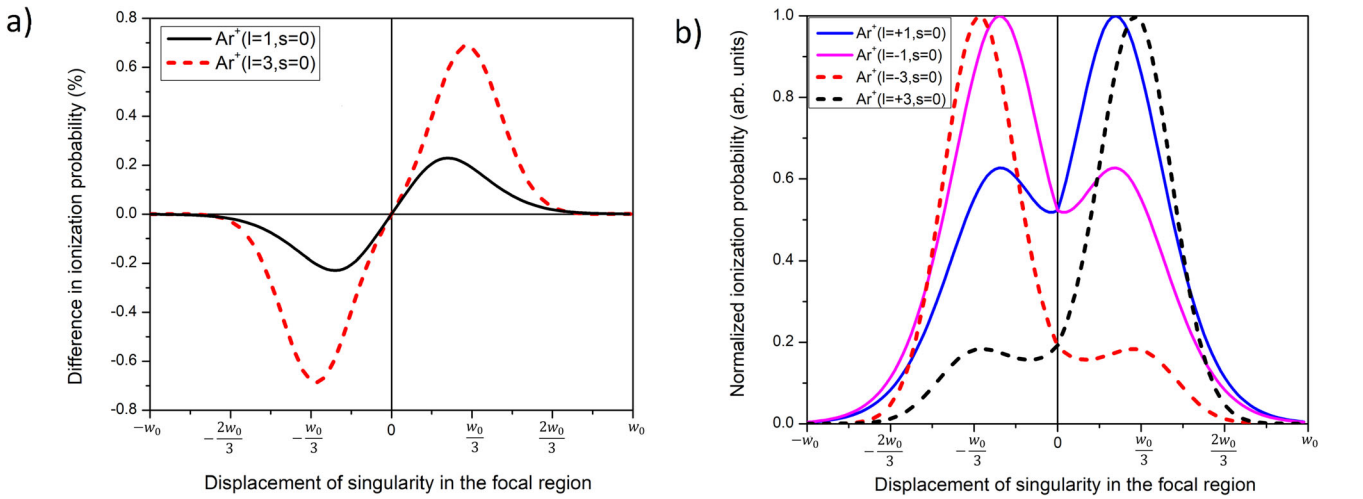

Fig. 4 | Simulated differential ionization probability of argon. a Simulated difference in ionization probabilities of argon between left- and right-helical light for $l = 1$ in black and $l = 3$ in red, respectively. **b** Single ionization probability of argon for $l = +1$ ($l = +3$) in blue (black) and $l = -1$ ($l = -3$) in magenta (red). They were obtained by solving Eq. (6) integrated over the beam cross-section for vertical polarization and intensity of 10^{14}W/cm^2 for $l = 1$ and 1.2×10^{14} W/cm^2 for $l = 3$. The x and y-axis are given in terms of the beam waist, $w_0 = 3\,\mu$m.

an additional control parameter to manipulate the molecular potential manifold and, therefore, the reaction dynamics. Additionally, the transverse spreading of the ionized electron wavepacket can be influenced, thereby affecting recollision dynamics (see Supplementary Fig. S11).

The peak field strength varies across the beam profile when the singularity is displaced in an OAM beam. It rises with δ and eventually reaches a maximum. As δ increases further, approaching the edge of the beam cross-section, the peak field strength decreases as the beam profile starts resembling that of a Gaussian beam. This variation in the peak field strength has a direct impact on the ponderomotive energy of the free electron, as depicted in Fig. 5a. At higher l-values, the null intensity region expands, and the field gradient intensifies. Consequently, the ponderomotive energy increases with l-value and reaches a maximum at smaller δ values. Similar enhancements in ponderomotive energy are feasible with synthesized light beams that do not have a helical phase. Such non-OAM beams can be produced by coherent superposition of Hermite-Gaussian beams with an intensity profile that resembles that of an asymmetric LG beam. However, the use of asymmetric LG beams offers a convenient knob to control ponderomotive effects instead of coherent superposition of multiple beams. While the increase in ponderomotive energy is mainly due to the intensity variation, the ionization modulation observed with OAM beams (Figs. 2–4) results from the interplay between the helical phase and field gradients. This becomes evident when the effects of the helical phase and field gradient are isolated by simulating the ionization probability for non-OAM structured light beams (see Supplementary Fig. S3). The probability exhibits a symmetrical double bump behavior due to the lack of OAM, in contrast to the asymmetry seen in Fig. 4b. Therefore, the helical phase can impact associated phenomena in strong-field physics.

In asymmetric LG beams, the multipole contributions couple from the carrier phase into the envelope, resulting in strong intensity modulations on the order of a wavelength. The carrier phase varies on a much shorter length scale than the electric field envelope. As such, the resulting multipole effects rooted in the carrier phase affect the ponderomotive force much stronger than the modulation of the pulse envelope alone. This is unique to OAM beams and is hard to achieve by methods that manipulate the envelope alone. So, phase singularity and field gradients are intertwined, as highlighted in the transition amplitude describing the tunnel ionization probability Eq. (4). It consists of two contributions: the electric quadrupole and magnetic dipole both in the pre-exponent and in the classical action via the vector potential gradient. The electric quadrupole (E1E2) in the pre-exponent affects only ionization and survives averaging for asymmetric beams. The non-dipole terms of the classical action in the exponential changes the electron trajectory - not important for ionization but for high harmonic generation (HHG) and acceleration.

The tunability of ponderomotive energy with asymmetric OAM beams significantly impacts HHG, a critical process in attosecond science. Transitioning from a Gaussian beam to an asymmetric OAM beam, at an intensity of 10^{14} W/cm^2, results in a threefold increase in ponderomotive energy for $l = 9$. This translates to extending the cut-off harmonics (3.17 U_p) by the same amount without the need for a laser operating at longer wavelengths. For example, an 800 nm asymmetric OAM beam would generate the same cut-off harmonics as a laser operating at 1500 nm with a Gaussian profile. Moreover, the drift energy of the electron (Up to $2U_p$), which is proportional to the ponderomotive energy, can be regulated by displacing the singularity within the transverse plane of the laser focus. However, the temporal electron dynamics in the laser field, *vis-à-vis* ionization and recollision times, remains the same for both Gaussian and OAM beams as shown in Fig. 5c. At a specific position of the singularity ($\delta = w_0/3$), the kinetic energy of the recolliding electron increases with l-value but its temporal dynamics is not influenced by the l-value or asymmetry parameter δ.

The controlled generation of electron wavepackets with asymmetric OAM beams also facilitates the probe of molecular dynamics by taking snapshots of conformational transformations. This is possible either by scattering of the electron wavepacket from its parent molecular ion (i) elastically, leading to a diffraction pattern, or (ii) inelastically, leading to multiple ionization and fragmentation from which changes to bond length and angles could be extracted. The ability to increase the ponderomotive energy of the electron with OAM beams enhances the spatial resolution in such studies.

Figure 5 b illustrates the variation of the average ponderomotive force in the focal plane as a function of the displacement of the singularity, δ, for different l-values. This force was obtained by integrating over the cross-section of the laser beam at the focus and depends on the gradient of the intensity. For a Gaussian beam, the average ponderomotive force is zero, represented by a circle. The behavior is similar for symmetric OAM beams. However, when the singularity is

https://doi.org/10.1038/s41467-025-57618-8

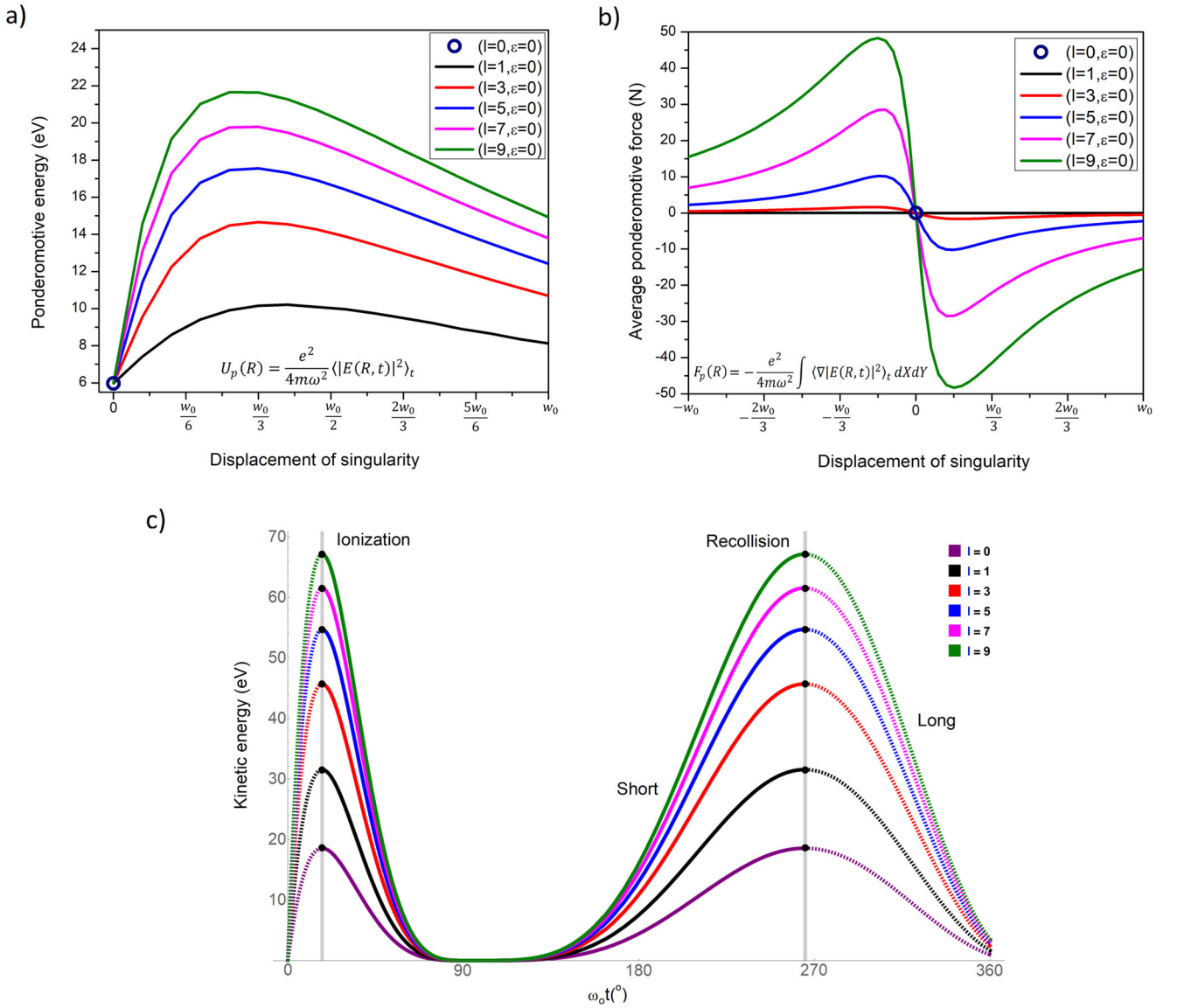

Fig. 5 | Tuning the ponderomotive energy and force. Simulation of (**a**) peak ponderomotive energy, and (**b**) average ponderomotive force, at an intensity of 10^{14} W/cm^2, for different positions of the singularity in a linearly polarized OAM beam and for different l-values. The open circles correspond to a Gaussian beam at the same laser intensity. The ponderomotive force was integrated over the beam cross-section at the laser focus. **c** Electron recollision dynamics in argon for $\delta = w_0/3$. The dash (solid) lines represent the long (short) trajectories created when the electron is ionized before (after) the peak located at $\omega_0 t' = 0.05 \times 2\pi = 18^\circ$. The electron will return to the parent ion at $\omega_0 t = 0.7 \times 2\pi = 252°$. The x and y-axis are given in terms of the beam waist ($w_0 = 3\,\mu$m) and the polarization in terms of ellipticity (ε).

displaced, the ponderomotive force exhibits local maxima and minima that increase with the l-value. The position of local maxima and minima in the ponderomotive force aligns with specific δ values where differential ionization exhibits maximum magnitude. In plasma physics, a factor of forty enhancement in ponderomotive force with asymmetric OAM beams facilitates the acceleration of charged particles to higher energies compared to Gaussian beams. This method serves as an alternate to the use of temporally asymmetric laser pulses to manipulate the characteristics of accelerated charged particles[40–42]. In addition, at a given intensity, l-dependent ionization of matter also enables to precisely control plasma density by an order of magnitude compared to a Gaussian beam. This could potentially be harnessed, for example, to manipulate laser filamentation and enhance its application in electromagnetic waveguiding and remote sensing of atmospheric molecules for accurate environmental monitoring.

Another application of asymmetric helical light pulses is towards super-resolution imaging due to their ability to localize and control light intensity to sub-wavelength dimensions. Figure 6a–d show the transverse intensity profiles for Gaussian and asymmetric LG beams in which the beam waist is fixed to the wavelength of light. As the OAM value increases, the light intensity is redistributed to a smaller bean-shaped area, and the peak intensity increases. Any nonlinear process, such as the multiphoton excitation of a fluorophore, exhibits a threshold intensity above which it emits radiation. By setting the threshold intensity at 90% we extracted the dimensions of the localized hot-spot and plotted it as a function of the OAM value, as shown in Fig. 6e. The size of the hot-spot is reduced by increasing the l-value with the x-dimension smaller than the y-dimension by a factor of two. Such localization can be combined with the ability to manipulate photoexcitation by changing the δ-position and helicity (as shown in Fig. 1b for ionization) to enhance the spatial resolution by a factor of 2–3 times the diffraction limit. This is a much simpler technique to create a localized hot-spot but is mostly restricted to one-dimension. This is in contrast to complicated methods such as hot-spot

https://doi.org/10.1038/s41467-025-57618-8

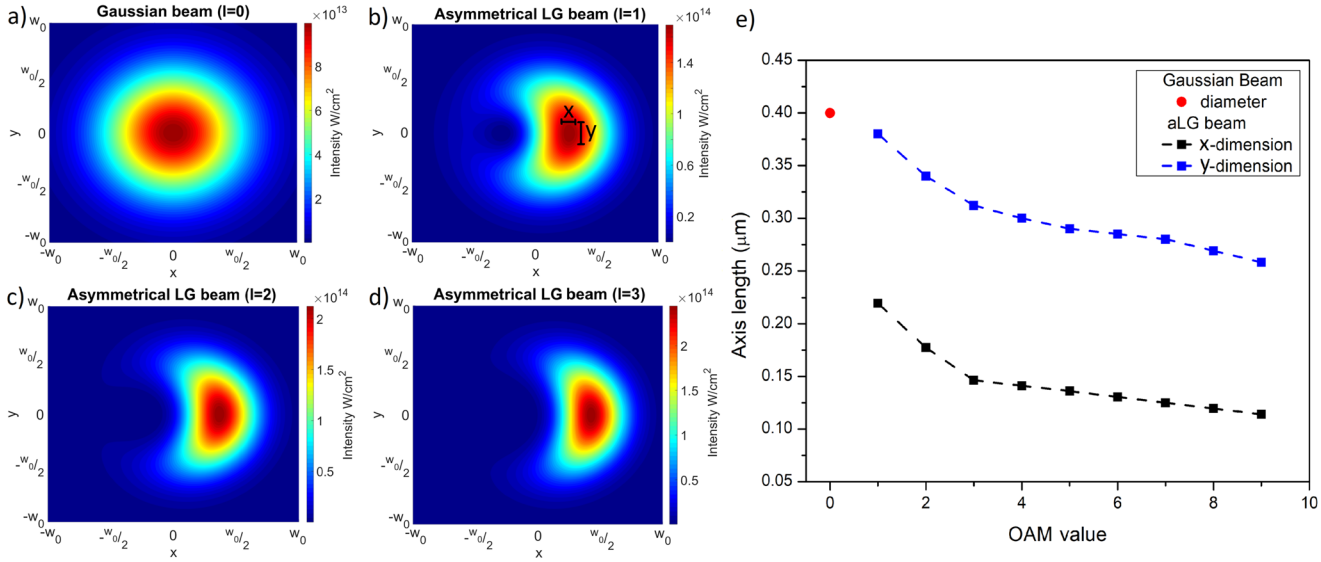

Fig. 6 | Field localization to achieve super-resolution. a–d Transverse intensity profiles of **a**) Gaussian, and **b**–**d**) asymmetric LG beams with $l = 1, 2, 3$ for $w_0 = \lambda$ and $\delta = w_0/3$. The dimensions of the intense central region in (**b**) represent a threshold intensity of 90%. **e** shows the x-dimension (black) and y-dimension (blue) of the intense region as a function of the OAM-value along with the Gaussian beam (red dot).

localization by the superposition of several coherent beams[43] or stimulated emission depletion involving two color coherent beams that require specially designed fluorophores that can be excited and deexcited[44,45].

In conclusion, we demonstrated l-dependent ionization of atoms and molecules that can be precisely controlled by manipulating the phase singularity within the OAM beam. We extended strong-field tunnel ionization beyond the dipole approximation to simulate the ionization of atoms. Our study provides valuable insight into the intricate mechanisms underlying strong-field physics. As discussed above, OAM beams provide an additional tool to manipulate extreme nonlinear processes that drive a spectrum of research domains. In spectroscopy, it allows us to probe conformational changes in molecules with enhanced spatial resolution. In attosecond science, it enables efficient generation of higher-order harmonics at shorter wavelengths. In plasma physics, it facilitates the efficient production of higher-energy charged particles. Additionally, by modifying the plasma density, laser filamentation can be effectively employed for remote sensing applications. In imaging, aysmmetric OAM beams enable us to localize photoexcitation of flourophores to achieve sub-wavelength spatial resolution.

Method

Ionization measurements

Experiments were conducted by focusing near-infrared femtosecond laser pulses with a parabolic mirror (focal length 5 cm) in the interaction region of a TOFMS housed inside a differentially pumped vacuum chamber. A Ti:Sapphire laser system (Spitfire, Spectra-Physics) operating at $\lambda = 800$ nm and a repetition rate of 1 KHz produced ~40 fs pulses with a maximum pulse energy of ~2.5 mJ. A combination of a half-wave plate and a polarizer were used to control the pulse energy. The pulse duration was continuously monitored by a single-shot autocorrelator. A fast photodiode was used to continuously monitor the laser pulse energy incident on a 3 mm thick quartz window on the vacuum chamber. The ions produced in the interaction region of TOFMS, operated in Wiley-McLaren geometry, travel through a field-free region of 30 cm after acceleration and are detected by a microchannel plate in chevron geometry. The signal is then amplified, discriminated, and recorded by a time digitizer to generate a TOF mass spectrum. The voltage on the microchannel plates was set at −4900 V. The voltages on the repeller and extractor plates of the mass spectrometer were +2000 V and +1000 V, respectively. A precision leak valve was used to introduce atoms and molecules in gas phase. The pressure inside the vacuum chamber was maintained at ~10^{-6} Torr. Organic compounds like limonene and acetone had sufficient vapor pressure, at room temperature, to be introduced as a gas. They were subjected to freeze-and-thaw cycles to minimize contamination of the interaction region. To minimize number density fluctuations, the chemicals in the glass vial were immersed in a temperature bath at 22 °C and the gas line along with the leak valve were maintained at a positive temperature gradient. The S(−)-limonene and R(+)-limonene were sourced from Sigma Aldrich with a purity of 96% and 97%, respectively. Measurements in limonene and acetone were performed at an intensity of $8–9 \times 10^{13}$ W/cm^2, below the measured saturation intensities of ~$12–13 \times 10^{13}$ W/cm^2. Measurements in argon were performed at an intensity of $9–15 \times 10^{13}$ W/cm^2. The differential ionization curves were obtained by displacing the position of singularity in the cross-section of the OAM beam. A pair of mass spectra, measured for 100,000 laser shots, were recorded for each handedness of the incident helical light. Fluctuations of the ion yields and error bars related to the differential ionization signal were computed based on repeated measurements under similar conditions.

Calibration of mass spectrometer, laser intensity and ellipticity

Mass calibration was achieved using Xenon atoms. Mass resolution of the spectrometer (full width at half maximum) was 550 at an m/z (mass-to-charge ratio) of 132. Laser intensity was calibrated by measuring the saturation intensity of argon. This was achieved by plotting Ar^+ yields as a function of pulse energy. The intercept on the energy axis of the semi-log plot corresponds to the theoretical saturation intensity of ~2.5×10^{14} W/cm^2. The extracted focal spot size in the interaction region was 3 ± 0.2 μm, in agreement with previous measurements. A quarter-wave plate (QWP) was used to change the ellipticity, ϵ, of the polarized helical light beam. It was calibrated by measuring the ellipticity dependence of doubly charged argon. We obtained $\epsilon = 0.05$ for linear polarization and $\epsilon = \pm 0.96$ for circular polarization, with an uncertainty of ± 0.02. The ellipticity was varied in steps of 0.04 around linear polarization and in steps of 0.08 beyond $\epsilon = 0.2$.

Generation of OAM beams and displacement of singularity

A QWP on a motorized rotation stage (with a ± 0.005° resolution) was used to generate circularly polarization light that was incident on a birefringent liquid-crystal-based phase plate called a q-plate. Circularly polarized Gaussian beam propagating through the q-plate with a topological charge q, acquires an OAM defined by $l = \pm 2q$, with a phase singularity and hence a null intensity region at the center of the beam, known as an optical vortex. The handedness of the incident circular polarization determines the direction of rotation of the wavefront structure *i. e.* the handedness of the helical light. A second QWP was used to generate linearly polarized OAM beams. The conversion efficiencies of the q-plates were ~86 ± 2% for $l = 1$ and ~88 ± 2% for $l = 3$. The singularity in the OAM beam was displaced by translating the q-plate across the incident beam, whose diameter was 12 mm. The q-plate, mounted on a motorized xy-translation stage with a precision of 10μm, was displaced in steps of 500 ± 10μm. When focused by the parabolic mirror, this translated to a displacement step size of 330 ± 60 nm in the interaction region with respect to the center of the beam. The calibration was achieved by measuring the total translation required to displace the singularity to the periphery of the defocused beam and comparing it to the measured spot size of $w_0 = 3 \pm 0.2\,\mu$m. An alternate method of displacing the singularity is by the coherent superposition of OAM beam with a tunable amount of a linearly polarized Gaussian beam[12]. The central singularity either shifts or unfolds into multiple singularities, depending on the topological charge of the q-plate. This shift can be precisely controlled by adjusting the external field applied to the q-plate. This action varies the optical retardation, thereby detuning the strength of the spin-to-orbital angular momentum coupling of light. A fraction of the input Gaussian beam co-propagates with a partially converted OAM beam.

Theory

Tunnel ionization of an atom is often described using SFA, where the laser field strength is comparable to the Coulomb field of an atom. It is predominant when the laser frequency is slower than the frequency of electron tunneling through the barrier. SFA assumes that only the ground state and the continuum are involved in the dynamics and that the intermediate states and ground state depletion are neglected.

Ionization probability can be obtained from the transition amplitude defined as a projection of the final state $\psi_f(t)$ to a fully evolved ground state at large times[32,33], given by $M_{fg} = \lim_{t\to\infty} \langle \psi_f(t)|\Psi(r,t)\rangle$, where $\Psi(r, t)$ is the total wave function of time-evolved ground state, ψ_g, when the laser field is turned on. $\Psi(r, t)$ is a solution of the time-dependent Schrodinger equation and is solved using the Green function $\hat{G}(t,t') = -i\Theta(t-t')\hat{U}(t,t')$[32,33] where $\Theta(t - t')$ is the Heaviside step function and $\hat{U}(t, t')$ is a unitary time operator. By using the orthogonality of the wavefunctions, the Born approximation where the perturbation acts only on the ground state, and approximating the final state as a Volkov wavefunction; $\langle\psi_f(t)|\hat{U}(t,t') \to \langle\psi_V(t')|$ we obtain the general SFA tunneling transition amplitude from the ground state to the continuum given by

$$M_{fg} = -i\int_{-\infty}^{\infty} dt' \langle \psi_V(t')|\hat{V}(t')|\psi_g(t')\rangle \tag{8}$$

In standard SFA, only the electric dipole moment is considered in the interaction Hamiltonian and in the Volkov wavefunction. In principle, the transition amplitude can be expressed either in velocity or length gauges. Conversion from one gauge to the other can be achieved by using the generating function $\chi(r,R,t) = \int_0^1 \vec{r}\cdot\vec{A}(R+\lambda r,t)d\lambda$ and its resulting unitary operator $e^{-i\chi(r,R,t)}$[46]. In the velocity gauge, the ground state wavefunction is given by $|\tilde{\psi}_g(t)\rangle = e^{-i\chi(r,R,t)}|\psi_g(t)\rangle$ and the Hamiltonian is given by $\hat{H}(t) = \frac{1}{2}\left(-i\vec{\nabla} + \vec{A}(r',t)\right)^2$ where $|\psi_g(t)\rangle$ is the ground state wavefunction in length gauge, $i\vec{\nabla}$ is the momentum operator and $\vec{A}(r', t)$ is the vector potential. We used the length gauge to derive the transition amplitude.

To introduce higher order multipoles in the interaction Hamiltonian, we

1. (i) Taylor expanded the vector potential to the second order about a point R in the interaction Hamiltonian as, $\vec{A}(r',t) \approx \vec{A}(R,t) + \vec{r}^{\,\mathrm{T}}\widehat{\partial A}(R,t)\ldots$, and in the generating function as, $A(R+\lambda r,t) = A(R,t) + \lambda\vec{r}^{\,\mathrm{T}}\widehat{\partial A}(R,t)$, where $\vec{r}^{\,\mathrm{T}}$ is the transpose of position vector.
2. (ii) Applied the unitary transformation operator $e^{-i\chi(r,R,t)}$ to explicitly express the existence of electric quadrupole and magnetic dipole in length gauge resulting in the non-dipole interaction Hamiltonian $\hat{V}(t') = r_i E_i(R,t') + \frac{1}{2}r_i r_j\widehat{\partial_j E_i}(R,t') + \frac{1}{2}L_i B_i(R,t')$, where $E_i(R, t)$ and $B_i(R, t)$ are the incident electric and magnetic fields, respectively, of the asymmetrical Laguerre-Gaussian laser beam (see Supplementary section 6), $r_{i,j}$ is the distance between positive and negative charge in the atomic frame and R represent the coordinates of the laser beam profile. $\widehat{\partial_j E_i}$ represents the field gradient, and L_i is the orbital angular momentum of the magnetic dipole transition moment.

Lastly, we expanded the Volkov wavefunction to include the higher order multipoles to $O(\widehat{\partial A})$ and converted it from velocity to length gauge using the first order transformation, $e^{-i\chi(r,R,t)} \sim e^{-iA(R,t)\cdot r}$ to obtain Eq. (3) of the main text (see Supplementary Section 5). The non-dipole free-electron wavefunction shown in Eq. (3) can be expressed in terms of time propagator, $\hat{U}_V(t,t')$, and a plane wave with a momentum $\pi(p,t,t')$

$$\Psi_V(r,t) = \frac{\hat{U}_V(t,t')}{(2\pi)^{3/2}}e^{i\pi(p,t,t')\cdot r} = \hat{U}_V(t,t')|\pi(p,t,t')\rangle \tag{9}$$

where

$$\pi(p,t,t') = \left(p + A(R,t') - \int_{t'}^{t}\widehat{\partial_R A}(R,\tau)[p + A(R,\tau)]d\tau\right);$$
$$\hat{U}_V(t,t') = e^{-\frac{i}{2}\int_{t'}^{t}\left(p + A(R,t'') - \int_{t''}^{t}\widehat{\partial_R A}(R,\tau)[p+A(R,\tau)]d\tau\right)^2 dt''}$$

Therefore, the length gauge ground state tunneling transition amplitude up to $O(\widehat{\partial A})$ becomes

$$M_{fg} = -i\int_{-\infty}^{t} dt' \langle\pi(p,t,t')|\hat{U}_V(t,t')V(t')|\psi_g(t')\rangle$$
$$= -i\int_{-\infty}^{t} dt' \langle\pi(p,t,t')|V(t')|\psi_g\rangle e^{iS(p,t,t')}$$

The full transition amplitude describing the tunnel ionization probability for an asymmetric Laguerre-Gaussian beam, shown in Equation (4) of the main text, can be obtained from

$$M_{fg} = -i\int_{-\infty}^{t} dt' \langle\pi(p,t,t')|r_i E_i(R,t') + \frac{1}{2}r_i r_j\widehat{\partial_j E_i}(R,t') + \frac{1}{2}L_i B_i(R,t')|\psi_g\rangle e^{iS(p,t,t')} \tag{10}$$

where

$$S(p,t,t') = \frac{1}{2}\int_{t'}^{t}\left[\left(p + A(t'') - \int_{t''}^{t}\widehat{\partial_R A}(p + A(\tau))d\tau\right)^2 + 2I_p\right]dt'' \tag{11}$$

To calculate the electric dipole, magnetic dipole, and electric quadrupole moment, we consider the ground state wave function of argon to be a 3p-orbital given by $|\psi_g(r)\rangle = R_{nl}(r)Y_{lm}(\theta,\phi) = |nlm\rangle$, where n, l, m are principal, orbital, and spin quantum numbers. These transition moments are expressed in the momentum space by applying the position operator on the momentum state to obtain

$$\begin{aligned}
&\mathrm{E1} = \langle\pi(p,t,t')|r_i|\psi_g(r,t')\rangle E_i(R,t') = i\partial_{\pi_i}|\psi_g(\boldsymbol{\pi}_\mathbf{p})\rangle E_i(R,t')\\
&\mathrm{E2} = \frac{1}{2}\langle\pi(p,t,t')|r_ir_j|\psi_g(r,t')\rangle\widehat{\partial_j E_i}(R,t') = -\frac{1}{2}\partial_{\pi_i}\partial_{\pi_j}|\psi_g(\boldsymbol{\pi}_\mathbf{p})\rangle\widehat{\partial_j E_i}(R,t')\\
&\mathrm{M1} = \frac{1}{2}\langle\pi(p,t,t')|L_i|\psi_g(r,t')\rangle B_i(R,t')\\
&\quad = \frac{1}{4}\begin{pmatrix}\sqrt{l(l+1)-m(m+1)}|\psi_{g(m+1)}(\boldsymbol{\pi}_\mathbf{p})\rangle + \sqrt{l(l+1)-m(m-1)}|\psi_{g(m-1)}(\boldsymbol{\pi}_\mathbf{p})\rangle\\ -i\sqrt{l(l+1)-m(m+1)}|\psi_{g(m+1)}(\boldsymbol{\pi}_\mathbf{p})\rangle + i\sqrt{l(l+1)-m(m-1)}|\psi_{g(m-1)}(\boldsymbol{\pi}_\mathbf{p})\rangle\\ m|\psi_g(\boldsymbol{\pi}_\mathbf{p})\rangle\end{pmatrix}B_i(R,t')
\end{aligned} \tag{12}$$

where the momentum wavefunction is defined as $|\psi_g(\boldsymbol{\pi}_\mathbf{p})\rangle = \langle\pi(p,t,t')|\psi_g(r,t')\rangle$ and $|\psi_{g(m\pm1)}(\boldsymbol{\pi}_\mathbf{p})\rangle = \langle\pi(p,t,t')|nl(m\pm1)\rangle$. The angular momentum operator is expressed in terms of the raising and lowering operators $(L_x = \frac{1}{2}(L_+ + L_-), L_y = \frac{1}{2i}(L_+ - L_-), L_z)$ and its definition on the spherical harmonics $L_\pm|nlm\rangle = \sqrt{l(l+1)-m(m\pm1)}|nl(m\pm1)\rangle$.

The momentum wavefunction was obtained by Fourier transforming the spatial radial wavefunction for hydrogen-like atoms[47].

$$\begin{aligned}
&FT[R_{nl}(r)] = F_{nl}(p) = \left[\frac{2}{\pi}\frac{(n-l-1)!}{(n+1)!}\right]^{(1/2)}\\
&n^2 2^{2(l+1)} l!\frac{n^l p^l}{(n^2p^2+1)^{l+2}}C_{n-l-1}^{l+1}\left(\frac{n^2p^2-1}{n^2p^2+1}\right)
\end{aligned} \tag{13}$$

where C_{n-l-1}^{l+1} is the Gegenbauer polynomial.

Therefore, the ground state wave function for argon (3p orbital, $n = 3$, $l = 1$, $m = 0, \pm1$) in momentum space is given by

$$\begin{aligned}
|\psi_{g(m=\pm1)}(\boldsymbol{\pi}_\mathbf{p})\rangle &= \underbrace{\frac{500}{\sqrt{\pi}}\boldsymbol{\pi}_\mathbf{p}\frac{(9\boldsymbol{\pi}_\mathbf{p}^2-1)}{(9\boldsymbol{\pi}_\mathbf{p}^2+1)^4}}_{F_{3,1}(\boldsymbol{\pi}_\mathbf{p})}\underbrace{\left[\mp\sqrt{\frac{3}{8\pi}}(\boldsymbol{\pi}_{p_x}\pm i\boldsymbol{\pi}_{p_y})\frac{1}{\boldsymbol{\pi}_\mathbf{p}}\right]}_{Y_{1,\pm1}(\theta,\phi)}\\
&= \mp\frac{34}{81\pi}(\boldsymbol{\pi}_{p_x}\pm i\boldsymbol{\pi}_{p_y})\frac{(\boldsymbol{\pi}_\mathbf{p}^2-2I_p)}{(\boldsymbol{\pi}_\mathbf{p}^2+2I_p)^4}\\
|\psi_{g(m=0)}(\boldsymbol{\pi}_\mathbf{p})\rangle &= \underbrace{\frac{500}{\sqrt{\pi}}\boldsymbol{\pi}_\mathbf{p}\frac{(9\boldsymbol{\pi}_\mathbf{p}^2-1)}{(9\boldsymbol{\pi}_\mathbf{p}^2+1)^4}}_{F_{3,1}(\boldsymbol{\pi}_\mathbf{p})}\underbrace{\left[\sqrt{\frac{3}{4\pi}}\frac{\boldsymbol{\pi}_{p_z}}{\boldsymbol{\pi}_\mathbf{p}}\right]}_{Y_{1,0}(\theta,\phi)} = \frac{3}{5\pi}(\boldsymbol{\pi}_{p_z})\frac{(\boldsymbol{\pi}_\mathbf{p}^2-2I_p)}{(\boldsymbol{\pi}_\mathbf{p}^2+2I_p)^4}
\end{aligned}$$

where $\sin\theta e^{(\pm i\phi)} = (\boldsymbol{\pi}_{p_x}\pm i\boldsymbol{\pi}_{p_y})\frac{1}{\boldsymbol{\pi}_\mathbf{p}}$, obtained by changing from spherical to Cartesian coordinates. The $\mp$ and $-$ symbols are associated to the magnetic quantum number (m) of the spherical harmonics and should not be confused with the superscript $\pm$ associated with the handedness of the electric and magnetic field of the asymmetric LG beams (Eqs. (1) and (7) see Supplementary Section 6).

The electric quadrupole was obtained by carrying out the differentiation.

$$\begin{aligned}
-\frac{1}{2}\partial_{\pi_i}\partial_{\pi_j}|\psi_g(\boldsymbol{\pi}_\mathbf{p})\rangle &= \pm\frac{17}{81\pi}\partial_{\pi_i}\left[-2(\boldsymbol{\pi}_{p_x}\pm i\boldsymbol{\pi}_{p_y})\boldsymbol{\pi}_{p_j}\frac{(3\boldsymbol{\pi}_\mathbf{p}^2-10I_p)}{(\boldsymbol{\pi}_\mathbf{p}^2+2I_p)^5}+\frac{(\boldsymbol{\pi}_\mathbf{p}^2-2I_p)}{(\boldsymbol{\pi}_\mathbf{p}^2+2I_p)^4}\left(\delta_{p_jp_x}\pm i\delta_{p_jp_y}\right)\right]\\
&= \pm\frac{17}{81\pi}\left[4(\boldsymbol{\pi}_{p_x}\pm i\boldsymbol{\pi}_{p_y})\boldsymbol{\pi}_{p_j}\boldsymbol{\pi}_{p_i}\frac{(-108\boldsymbol{\pi}_\mathbf{p}^2I_p+50I_p+21\boldsymbol{\pi}_\mathbf{p}^4)}{(\boldsymbol{\pi}_\mathbf{p}^2+2I_p)^6}\right.\\
&\quad\left.-2\frac{(3\boldsymbol{\pi}_\mathbf{p}^2-10I_p)}{(\boldsymbol{\pi}_\mathbf{p}^2+2I_p)^5}\left[\left(\delta_{p_ip_x}\pm i\delta_{p_ip_y}\right)\boldsymbol{\pi}_{p_j}+\delta_{p_ip_j}\left(\boldsymbol{\pi}_{p_x}\pm i\boldsymbol{\pi}_{p_y}\right)+\left(\delta_{p_jp_x}\pm i\delta_{p_jp_y}\right)\boldsymbol{\pi}_{p_i}\right]\right]
\end{aligned} \tag{14}$$

Therefore, the electric dipole, electric quadrupole, and magnetic dipole terms for the argon atom are given by the below three equations.

$$\begin{aligned}
\mathrm{E1} &= \langle\pi(\mathbf{p})|r_i|\psi_g(r)\rangle E_i(R) =\\
&\mp i\frac{34}{81\pi}\left[-2(\boldsymbol{\pi}_{p_x}\pm i\boldsymbol{\pi}_{p_y})\boldsymbol{\pi}_{p_j}\frac{(3\boldsymbol{\pi}_\mathbf{p}^2-10I_p)}{(\boldsymbol{\pi}_\mathbf{p}^2+2I_p)^5}+\frac{(\boldsymbol{\pi}_\mathbf{p}^2-2I_p)}{(\boldsymbol{\pi}_\mathbf{p}^2+2I_p)^4}\left(\delta_{p_jp_x}\pm i\delta_{p_jp_y}\right)\right]E_i(R)
\end{aligned} \tag{15}$$

$$\begin{aligned}
\mathrm{E2} &= \frac{1}{2}\langle\boldsymbol{\pi}(\mathbf{p})|r_ir_j|\psi_g(r)\rangle\widehat{\partial_j E_i}(R)\\
&= \pm\frac{17}{81\pi}\left[4(\boldsymbol{\pi}_{p_x}\pm i\boldsymbol{\pi}_{p_y})\boldsymbol{\pi}_{p_j}\boldsymbol{\pi}_{p_i}\frac{(-108\boldsymbol{\pi}_\mathbf{p}^2I_p+50I_p+21\boldsymbol{\pi}_\mathbf{p}^4)}{(\boldsymbol{\pi}_\mathbf{p}^2+2I_p)^6}\right.\\
&\quad-2\frac{(3\boldsymbol{\pi}_\mathbf{p}^2-10I_p)}{(\boldsymbol{\pi}_\mathbf{p}^2+2I_p)^5}\left[\left(\delta_{p_ip_x}\pm i\delta_{p_ip_y}\right)\boldsymbol{\pi}_{p_j}+\delta_{p_ip_j}\left(\boldsymbol{\pi}_{p_x}\pm i\boldsymbol{\pi}_{p_y}\right)\right.\\
&\quad\left.\left.+\left(\delta_{p_jp_x}\pm i\delta_{p_jp_y}\right)\boldsymbol{\pi}_{p_i}\right]\right]\widehat{\partial_j E_i}(R)
\end{aligned} \tag{16}$$

$$\begin{aligned}
\mathrm{M1} &= \frac{1}{2}\langle\boldsymbol{\pi}(\mathbf{p})|L_i|\psi_g(r)\rangle B_i(R)\\
&= i\frac{34}{81\pi\sqrt{2}}\frac{(\boldsymbol{\pi}_\mathbf{p}^2-2I_p)}{(\boldsymbol{\pi}_\mathbf{p}^2+2I_p)^4}\left[-\boldsymbol{\pi}_{p_y}B_x(R)+\boldsymbol{\pi}_{p_x}B_y(R)\right]
\end{aligned} \tag{17}$$

Using partial fraction expansion, the above expressions for the electric dipole, electric quadrupole, and magnetic dipole of argon can be rewritten as

$$\begin{aligned}
\mathrm{E1} &= \langle\pi(\mathbf{p})|r_i|\psi_g(r)\rangle E_i(R)\\
&= \pm i\frac{68}{81\pi}(\boldsymbol{\pi}_{p_x}\pm i\boldsymbol{\pi}_{p_y})\boldsymbol{\pi}_{p_j}\left(\frac{1}{(\boldsymbol{\pi}_\mathbf{p}^2+2I_p)^4}-\frac{16I_p}{3(\boldsymbol{\pi}_\mathbf{p}^2+2I_p)^5}\right)E_i(R)\\
&\quad\mp i\frac{34}{81\pi}\left(\frac{1}{(\boldsymbol{\pi}_\mathbf{p}^2+2I_p)^3}-\frac{4I_p}{(\boldsymbol{\pi}_\mathbf{p}^2+2I_p)^4}\right)\left(\delta_{p_jp_x}\pm i\delta_{p_jp_y}\right)E_i(R)
\end{aligned} \tag{18}$$

$$\begin{aligned}
\mathrm{E2} &= \frac{1}{2}\langle\boldsymbol{\pi}(\mathbf{p})|r_ir_j|\psi_g(r)\rangle\widehat{\partial_j E_i}(R) = \pm\frac{17}{81\pi}\left[4(\boldsymbol{\pi}_{p_x}\pm i\boldsymbol{\pi}_{p_y})\boldsymbol{\pi}_{p_j}\boldsymbol{\pi}_{p_i}\left(\frac{(50(6I_p^2+I_p)}{(\boldsymbol{\pi}_\mathbf{p}^2+2I_p)^6}-\frac{192I_p}{(\boldsymbol{\pi}_\mathbf{p}^2+2I_p)^5}+\frac{21}{(\boldsymbol{\pi}_\mathbf{p}^2+2I_p)^4}\right)\right.\\
&\quad\left.-2\left(\frac{1}{(\boldsymbol{\pi}_\mathbf{p}^2+2I_p)^4}-\frac{16I_p}{3(\boldsymbol{\pi}_\mathbf{p}^2+2I_p)^5}\right)\left[\left(\delta_{p_ip_x}\pm i\delta_{p_ip_y}\right)\boldsymbol{\pi}_{p_j}+\delta_{p_ip_j}\left(\boldsymbol{\pi}_{p_x}\pm i\boldsymbol{\pi}_{p_y}\right)+\left(\delta_{p_jp_x}\pm i\delta_{p_jp_y}\right)\boldsymbol{\pi}_{p_i}\right]\right]\widehat{\partial_j E_i}(R)
\end{aligned} \tag{19}$$

$$\begin{aligned}
\mathrm{M1} &= \frac{1}{2}\langle\boldsymbol{\pi}(\mathbf{p})|L_i|\psi_g(r)\rangle B_i(R) = i\frac{34}{81\pi\sqrt{2}}\left(\frac{1}{(\boldsymbol{\pi}_\mathbf{p}^2+2I_p)^3}-\frac{4I_p}{(\boldsymbol{\pi}_\mathbf{p}^2+2I_p)^4}\right)\\
&\quad\left[-\boldsymbol{\pi}_{p_y}B_x(R)+\boldsymbol{\pi}_{p_x}B_y(R)\right]
\end{aligned} \tag{20}$$

These three terms were substituted in transition amplitude (Eq. (4) of the main text), and the time integral was solved by saddle point integration using the method of steepest descent (stationary phase method)[48–50]. The resultant transition amplitude has the form $M_{fg} = -i\int_C g(p,t,t')e^{iS(p,t,t')}dt'$ where $g(p,t,t') = \langle\pi(p,t,t')|\hat{V}(R,r,t')|\psi_g(t')\rangle$ represents the transition matrix element from the ground state to the continuum. It contains 11 terms; 4 for electric dipole, 5 for electric quadrupole, and 2 for the magnetic dipole, respectively, as shown in the above two equations. Each term has a generic form $\sim\frac{\zeta_i(p,t,t')}{(2I_p+\pi^2(p,t,t'))^n}$ where $n = 3, 4, 5$ for electric dipole, $n = 4, 5, 6$ for electric quadrupole, and $n = 3, 4$ for the magnetic dipole. $\zeta_i(p,t,t')$ is the numerator specific to each term. $g(p,t,t')$ varies slowly compared to the fast oscillating function $e^{iS(p,t,t')}$, so the integral averages to zero unless there are regions where the phase of the oscillation, $S(p,t,t')$, stays nearly constant. In other words, areas around the point where the derivative of the function in the phase goes to zero, *i.e.* $\frac{\partial}{\partial t'}S(p,t,t') = 0 = S'(p,t,t')$. This

occurs at a saddle point t_s where $S'(p,t,t') = 2I_p + \pi^2(p,t,t') = 0$. As a result, all the terms in electric dipole, magnetic dipole, and electric quadrupole transitions contain a singularity at the saddle point t_s.

To solve the transition amplitude M_{fg}, we Taylor expand $S(p,t,t') \approx S(p,t,t_s) + \frac{1}{2}S''(p,t,t_s)(t'-t_s)^2$ around the saddle point, and substitution gives the below generic expression for each of the 11 terms involved in electric dipole, magnetic dipole, and electric quadrupole transitions

$$M_{fg}(p,t) = -i\zeta_i(p,t,t_s)e^{iS(p,t,t_s)}e^{i\phi}\int_{C'}\frac{1}{S'(p,t,t')^n}e^{i\frac{1}{2}S''(p,t,t_s)\epsilon^2}d\epsilon \quad (21)$$

where the deformed contour C' is going through the saddle point as a straight line at an angle ϕ.

To handle the singularity in the denominator in the vicinity of the saddle point t_s we approximated the term to $S'(p,t,t_s) = S''(p,t,t_s)(t'-t_s)$[48,49], leading to

$$M_{fg}(p,t) = -i\frac{\zeta(p,t,t_s)}{S''(p,t,t_s)^n}e^{iS(p,t,t_s)}e^{i\phi}\int_{C'}\frac{1}{(t'-t_s)^n}e^{i\frac{1}{2}S''(p,t,t_s)(t'-t_s)^2}dt' \quad (22)$$

Substituting the definition of Gamma function in the transition amplitude, $\frac{\Gamma(n)}{(t'-t_s)^n} = \int_0^\infty x^{n-1}e^{-x(t'-t_s)}dx$, leads to a double integral given by

$$M_{fg}(p,t) = -i\frac{\zeta_i(p,t,t_s)}{S''(p,t,t_s)^n}e^{iS(p,t,t_s)}e^{i\phi}\int_0^\infty\frac{x^{n-1}}{\Gamma(n)}\left[\int e^{i\frac{1}{2}S''(p,t,t_s)(t'-t_s)^2}e^{-x(t'-t_s)}dt'\right]dx \quad (23)$$

To solve this we applied a change of variable $\epsilon = (t'-t_s)$, to get

$$M_{fg}(p,t) = -i\frac{\zeta_i(p,t,t_s)}{S''(p,t,t_s)^n}e^{iS(p,t,t_s)}e^{i\phi}\int_0^\infty\frac{x^{n-1}}{\Gamma(n)}\left[\underbrace{\int e^{-\left(-i\frac{1}{2}S''(p,t,t_s)\epsilon^2+x\epsilon\right)}d\epsilon}_{I}\right]dx \quad (24)$$

in which the time integral $I = \int e^{-\left(-i\frac{1}{2}S''(p,t,t_s)\epsilon^2+x\epsilon+\lambda^2-\lambda^2\right)}d\epsilon = e^{\lambda^2}\int e^{-(a\epsilon+\lambda)^2}d\epsilon = e^{\lambda^2}\frac{\sqrt{\pi}}{a}$ where $a = \sqrt{-i\frac{1}{2}S''(p,t,t_s)}$ and $\lambda = \frac{x}{2\sqrt{-i\frac{1}{2}S''(p,t,t_s)}} = \tilde{\lambda}x$.

Substituting the time integral I in Eq. (24), using $\int_0^\infty x^{n-1}e^{\tilde{\lambda}^2x^2}dx = \frac{\Gamma(n/2)}{2}\left(-\frac{1}{\tilde{\lambda}^2}\right)^{n/2}$ and rearranging leads to

$$M_{fi}(p,t) = -i\frac{\Gamma(n/2)}{2\Gamma(n)}\zeta_i(p,t,t_s)\sqrt{\frac{2i\pi}{S''(p,t,t_s)}}\left(\frac{2i}{S''(p,t,t_s)}\right)^{n/2}e^{iS(p,t,t_s)}e^{i\phi} \quad (25)$$

We retain only the odd values of $(n = 2k+1)$ since they result in a non-zero residue from series expansion over the contour integral of Eq. (22).

$$M_{fi}(p,t) = -i\sqrt{\pi}\frac{\Gamma((2k+1)/2)}{2\Gamma(2k+1)}\zeta_i(p,t,t_s)\left(\frac{2i}{S''(p,t,t_s)}\right)^{k+1}e^{iS(p,t,t_s)}e^{i\phi} \quad (26)$$

We replace $\zeta_i(p,t,t_s)$ for the electric dipole, electric quadrupole, and magnetic dipole moments with their respective terms for $n = 3$ and $n = 5$ given in Eqs. (18)–(20) to get

$$M_{fg}(p,t) = 2i\sqrt{\pi}\frac{\Gamma(3/2)}{\Gamma(3)}\left(\frac{\zeta_i(p,t,t_s)}{S''(p,t,t_s)^2}\right)e^{iS(p,t,t_s)}e^{i\phi};$$
$$M_{fg}(p,t) = -4\sqrt{\pi}\frac{\Gamma(5/2)}{\Gamma(5)}\left(\frac{\zeta_i(p,t,t_s)}{S''(p,t,t_s)^3}\right)e^{iS(p,t,t_s)}e^{i\phi} \quad (27)$$

The full transition moment after integration is given by

$$M_{fg}^{\mathrm{E1}}(p,t) = \pm\frac{68}{81\sqrt{\pi}}\left[4i\frac{\Gamma(5/2)}{\Gamma(5)}(\boldsymbol{\pi}_{p_x}\pm i\boldsymbol{\pi}_{p_y})\boldsymbol{\pi}_{p_i}\left(\frac{16I_p}{3S''(p,t,t_s)^3}\right) + \frac{\Gamma(3/2)}{\Gamma(3)}\left(\frac{1}{S''(p,t,t_s)^2}\right)\left(\delta_{p_ip_x}\pm i\delta_{p_ip_y}\right)\right]E_i(R)e^{iS(p,t,t_s)}e^{i\phi} \quad (28)$$

$$M_{fg}^{\mathrm{E2}}(p,t) = \pm\frac{68}{81\sqrt{\pi}}\frac{\Gamma(5/2)}{\Gamma(5)}\left[4(\boldsymbol{\pi}_{p_x}\pm i\boldsymbol{\pi}_{p_y})\boldsymbol{\pi}_{p_j}\boldsymbol{\pi}_{p_i}\left(\frac{192I_p}{S''(p,t,t_s)^3}\right) - 2\left(\frac{16I_p}{3S''(p,t,t_s)^3}\right)\left[\left(\delta_{p_ip_x}\pm i\delta_{p_ip_y}\right)\boldsymbol{\pi}_{p_j} + \delta_{p_ip_j}\left(\boldsymbol{\pi}_{p_x}\pm i\boldsymbol{\pi}_{p_y}\right) + \left(\delta_{p_jp_x}\pm i\delta_{p_jp_y}\right)\boldsymbol{\pi}_{p_i}\right]\right]\widehat{\partial_j E_i}(R)e^{iS(p,t,t_s)}e^{i\phi} \quad (29)$$

$$M_{fg}^{\mathrm{M1}}(p,t) = \frac{68}{81\sqrt{2\pi}}\frac{\Gamma(3/2)}{\Gamma(3)}\left(\frac{1}{S''(p,t,t_s)^2}\right)\left(\boldsymbol{\pi}_{p_y}B_x(R) - \boldsymbol{\pi}_{p_x}B_y(R)\right)e^{iS(p,t,t_s)}e^{i\phi} \quad (30)$$

For linearly polarized light to $O(\widehat{\partial A})$, $S''(p,t,t_s)$ can be written as

$$S''(p,t,t_s) = -2i\sqrt{2I_p}E_i(t_s)\left[1+\int_{t_s}^{t}\partial_i A_i(\tau)d\tau\right] \quad (31)$$

At the saddle point $\frac{\partial}{\partial t'}S(p,t,t') = 0 \Rightarrow (p+A(t'))^2 - \int_{t'}^{t}\widehat{\partial}_R A(\tau)(p+A(\tau))d\tau)^2 = -2I_p$, this expression describes tunneling. It shows that the electron kinetic energy at time t' is negative, its velocity is complex and hence the time $t' = t_s \pm i\eta$. The time t' can be identified with the moment when the electron enters the barrier. Its real part t_s will then correspond to the time when the electron exits the barrier. Substituting the complex time at the saddle point, regrouping real and imaginary terms in $S(p,t,t')$ and after variable transformation $(\tau' = \frac{t''}{2} = t_s;\ d\tau' = dt''$ and taking $t_s \to 0$ and $t' \to \pm i\eta)$ and neglecting $O(\widehat{\partial A})$ terms we get

$$iS(p,t,t_s) = \frac{i}{2}\int_{t_s\pm i\eta}^{t}dt''\left(\pi^2(p,t,t'')+2I_p\right) = \frac{i}{2}\left[\int_{t_s}^{t}\left(\pi^2(p,t,t'')dt''+2I_p\right) - \int_0^{\pm i\eta}\left(\pi^2(p,t,\tau')+2I_p\right)d\tau'\right] \quad (32)$$

$$iS(p,t,t_s) = -\frac{(2I_p)^{3/2}}{3E_i(t_s)}\left(1+\frac{3}{4I_p}\sum_{j\neq i}\left[p_j+\frac{2I_p}{3E_i(t_s)}\partial_j A_i(t_s) - \int_{t_s}^{t}d\tau(A_i(\tau)-A_i(t_s))\partial_j A_i(\tau)\right]^2\right) \quad (33)$$

From the saddle point method, we can represent the momentum in terms of the ionization potential $\boldsymbol{\pi}_p = i\sqrt{2I_p}$. For elliptical light, the momentum components takes the form $\boldsymbol{\pi}_{p_x} = \alpha\boldsymbol{\pi}_p$ and $\boldsymbol{\pi}_{p_y} = i\beta\boldsymbol{\pi}_p$ where α, β are the polarization factors. By considering only the

normalized field amplitude for the dominant first order term in $iS(p, t, t_s)$ and $S''(p, t, t_s)$, the non-dipole total transition probability can be calculated using

$$\overline{P}_{fg} = \int_{-w_0}^{w_0} \left| M_{fg}^{\mathrm{E1}} + M_{fg}^{\mathrm{E2}} + M_{fg}^{\mathrm{M1}} \right|^2 dR \tag{34}$$

to describe the ionization probability over the interaction region shown in Fig. 4b and the difference in the probability corresponding to HD defined as $\Delta\overline{P}_{fg} = \overline{P}_{fg}(+l) - \overline{P}_{fg}(-l)$ shown in Fig. 4a.

Data availability

The minimum dataset necessary to interpret the results can be obtained from the corresponding authors upon request. The raw and processed data are not deposited in a repository because, without proper context, the data could be hard to interpret.

Code availability

The simulation data were obtained by evaluating the equations using standard technical software. The code is available upon request to the corresponding authors.

References

1. Forbes, A. et al. Structured light. *Nat. Photon.* **15**, 253–262 (2021).
2. He, C., Shen, Y. & Forbes, A. Towards higher-dimensional structured light. *Light Sci. Appl.* **11**, 205 (2022).
3. Padgett, M. & Bowman, R. Tweezers with a twist. *Nat. Photon.* **5**, 343–348 (2011).
4. Taylor, M. et al. Enhanced optical trapping via structured scattering. *Nat. Photon.* **9**, 669–673 (2015).
5. Fickler, R. Quantum entanglement of high angular momenta. *Science* **338**, 640–643 (2012).
6. Krenn, M. et al. Generation and confirmation of a (100 × 100)-dimensional entangled quantum system. *Proc. Natl. Acad. Sci.* **111**, 6243–6247 (2014).
7. Wang, J. et al. Terabit free-space data transmission employing orbital angular momentum multiplexing. *Nat. Photon.* **6**, 488–496 (2012).
8. Bozinovic, N. et al. Terabit-scale orbital angular momentum mode division multiplexing in fibers. *Science* **340**, 1545–1548 (2013).
9. Shi, Z. et al. Super-resolution orbital angular momentum holography. *Nat. Commun.* **14**, 1869 (2023).
10. Toyoda, K. et al. Using optical vortex to control the chirality of twisted metal nanostructures. *Nano Lett.* **12**, 3645–3649 (2012).
11. Ambrosio, A. et al. Light-induced spiral mass transport in azo-polymer films under vortex-beam illumination. *Nat. Commun.* **3**, 989 (2012).
12. Rahimian, M. G. et al. Spatially controlled nano-structuring of silicon with femtosecond vortex pulses. *Sci. Rep.* **10**, 12643 (2020).
13. Alameer, M. et al. Mapping complex polarization states of light on a solid. *Opt. Lett.* **44**, 5757 (2018).
14. Kylstra, N. J., Potvliege, R. M. & Joachain, C. J. Photon emission by ions interacting with short intense laser pulses: beyond the dipole approximation. *J. Phys. B: At. Mol. Opt. Phys.* **34**, L55 (2001).
15. Maurer, J. & Keller, U. Ionization in intense laser fields beyond the electric dipole approximation: concepts, methods, achievements and future directions. *J. Phys. B: At. Mol. Opt. Phys* **54**, 094001 (2021).
16. Cireasa, R. et al. Probing molecular chirality on a sub-femtosecond timescale. *Nat. Phys.* **11**, 654 (2015).
17. Bégin, J. L. et al. Nonlinear helical dichroism in chiral and achiral molecules. *Nat. Photon.* **17**, 82–88 (2023).
18. Jain, A. et al. Intrinsic dichroism in amorphous and crystalline solids with helical light. *Nat. Commun.* **15**, 1350 (2024).
19. Picon, A. et al. Photoionization with orbital angular momentum beams. *Opt. Exp.* **18**, 3660–3671 (2010).
20. Schmiegelow, C. T. et al. Transfer of optical orbital angular momentum to a bound electron. *Nat. Commun.* **7**, 12998 (2016).
21. Afanasev, A. et al. Experimental verification of position-dependent angular-momentum selection rules for absorption of twisted light by a bound electron. *New J. Phys.* **20**, 023032 (2018).
22. Kong, F. et al. Controlling the orbital angular momentum of high harmonic vortices. *Nat. Commun.* **8**, 14970 (2017).
23. Dorney, K. M. et al. Controlling the polarization and vortex charge of attosecond high-harmonic beams via simultaneous spin–orbit momentum conservation. *Nat. Photon.* **13**, 123–130 (2019).
24. Rego, L. et al. Generation of extreme-ultraviolet beams with time-varying orbital angular momentum. *Science* **364**, 6447 (2019).
25. Keren-Zur, S. et al. Generation of spatiotemporally tailored terahertz wavepackets by nonlinear metasurfaces. *Nat. Commun.* **10**, 1778 (2019).
26. Jana, K. et al. Quantum control of flying doughnut terahertz pulses. *Sci. Adv.* **10**, 2 (2024).
27. Kubel, M. et al. Strong-field control of the dissociative ionization of N_2O with near-single-cycle pulses. *New J. Phys.* **16**, 065017 (2014).
28. Li, S. et al. Pulse shaping in strong-field ionization: Theory and experiments. *Phys. Rev. A* **105**, 053105 (2022).
29. Hart, N. A. et al. Selective strong-field enhancement and suppression of ionization with short laser pulses. *Phys. Rev. A* **93**, 063426 (2016).
30. Kaufman, B. et al. Coherent control of internal conversion in strong-field molecular ionization. *Phys. Rev. Lett.* **125**, 053202 (2020).
31. Chaloupka, J. L. & Hickstein, D. D. Dynamics of strong-field double ionization in two-color counterrotating fields. *Phys. Rev. Lett.* **116**, 143005 (2016).
32. Long, Z. J. & Liu, W.-K. Keldysh theory of strong-field ionization. *Can. J. Phys.* **88**, 4, (2010).
33. Reiss, H. R. Theoretical methods in quantum optics: S-matrix and Keldysh techniques for strong-field processes. *Prog. Quant. Electr.* **16**, 1–71 (1992).
34. Lembessiss, V. E. & Babiker, M. Enhanced quadrupole effects for atoms in optical vortices. *Phys. Rev. Lett.* **110**, 083002 (2013).
35. Derevianko, A. Hyperfine-induced quadrupole moments of alkali-metal-atom ground states and their implications for atomic clocks. *Phys. Rev. A* **93**, 012503 (2016).
36. Kozhedub, Y. S. & Shabaev, V. M. Relativistic theory of the electric quadrupole moment of a hydrogen-like atom in the $s_{1/2}$ and $p_{1/2}$ states. *Opt. Spectrosc.* **99**, 527–535 (2005).
37. Amusia, M. Y., Kuchiev, M. Y. & Yakhontov, V. L. Quadrupole moment of atoms with the ground-state term $P_{1/2}$. *J. Phys. B: Atom. Mol. Phys.* **19**, L541 (1986).
38. Powis, I. et al. A valence photoelectron imaging investigation of chiral asymmetry in the photoionization of Fenchone and Camphor. *Chem. Phys. Chem.* **9**, 475 (2008).
39. Lux, C. et al. Circular Dichroism in the photoelectron angular distributions of camphor and fenchone from multiphoton ionization with femtosecond laser pulses. *Angew. Chem. Int. Ed.* **51**, 5001 (2012).
40. Leemans, W. P. et al. Electron-yield enhancement In A Laser-Wakefield accelerator driven by asymmetric laser pulses. *Phys. Rev. Lett.* **89**, 174802 (2002).
41. Sedaghat, M., Amouye Foumani, A. & Niknam, A. R. Controlling the characteristics of injected and accelerated electron bunch in corrugated plasma channel by temporally asymmetric laser pulses. *Sci. Rep.* **12**, 8115 (2022).
42. Huijts, J. et al. Waveform control of relativistic electron dynamics in laser-plasma acceleration. *Phys. Rev. X* **12**, 011036 (2022).
43. Liu, T. et al. Picophotonic localization metrology beyond thermal fluctuations. *Nat. Mater.* **22**, 844–847 (2023).

44. Hell, S. W. & Wichmann, J. Breaking the diffraction resolution limit by stimulated emission: stimulated-emission-depletion fluorescence microscopy. *Opt. Lett.* **19**, 80–782 (1994).
45. Rittweger, E. et al. STED microscopy reveals crystal colour centres with nanometric resolution. *Nat. Photon.* **3**, 144–147 (2009).
46. Frutak, J. et al. The multipole expansion in quantum theory. *Can. J. Phys.* **41**, 12 (1963).
47. Bethe, H. A. & Salpeter, E. E. *Quantum mechanics of one- and two electron atoms.* (Springer · Verlag Berlin Heidelberg, New York, 1957).
48. Gribakin, G. F. & Kuchiev, M. Y. Multiphoton detachment of electrons from negative ions. *Phys. Rev. A* **55**, 3760 (1997).
49. Kjeldsen, T. K. & Madsen, L. B. Strong-field ionization of atoms and molecules: The two-term saddle-point method. *Phys. Rev. A* **74**, 023407 (2006).
50. Smirnova, O. & Ivanov, M. Multielectron high harmonic generation: Simple man on a complex plane. In Attosecond and XUV Physics (eds T. Schultz and M. Vrakking) (2014).

Acknowledgements

We thank PhD student Felix Hufnagel from Prof. Karimi's group for fabricating the q-plate used in the experiments. We thank PhD student Ashish Jain for his valuable discussion and input. We also acknowledge financial support from the Natural Science and Engineering Council of Canada, Canada Research Chairs, and the Canadian Foundation for Innovation.

Author contributions

J.-L.B. and R.B. conceived, designed, and planned the experiments. J.-L.B. conducted the experiments and analyzed the results. T.B. developed the theory, and J.-L.B. and R.B. worked on the theory and conducted numerical simulations. J.-L.B., T.B., and R.B. prepared the first draft, and E.K. and P.C. reviewed the manuscript.

Competing interests

The authors declare no competing interest.

Additional information

Supplementary information The online version contains supplementary material available at https://doi.org/10.1038/s41467-025-57618-8.

Correspondence and requests for materials should be addressed to Jean-Luc Bégin, Thomas Brabec or Ravi Bhardwaj.

Peer review information *Nature Communications* thanks the anonymous reviewer(s) for their contribution to the peer review of this work. A peer review file is available.